

Accepted Manuscript

Title: Catalytic performance of bulk and colloidal Co/Al layered double hydroxide with Au nanoparticles in aerobic olefin oxidation

Authors: Sónia R. Leandro, Cristina I. Fernandes, Ana S. Viana, Ana C. Mourato, Pedro D. Vaz, Carla D. Nunes



PII: S0926-860X(19)30310-2
DOI: <https://doi.org/10.1016/j.apcata.2019.117155>
Article Number: 117155

Reference: APCATA 117155

To appear in: *Applied Catalysis A: General*

Received date: 15 May 2019
Revised date: 16 July 2019
Accepted date: 17 July 2019

Please cite this article as: Leandro SR, Fernandes CI, Viana AS, Mourato AC, Vaz PD, Nunes CD, Catalytic performance of bulk and colloidal Co/Al layered double hydroxide with Au nanoparticles in aerobic olefin oxidation, *Applied Catalysis A, General* (2019), <https://doi.org/10.1016/j.apcata.2019.117155>

This is a PDF file of an unedited manuscript that has been accepted for publication. As a service to our customers we are providing this early version of the manuscript. The manuscript will undergo copyediting, typesetting, and review of the resulting proof before it is published in its final form. Please note that during the production process errors may be discovered which could affect the content, and all legal disclaimers that apply to the journal pertain.

Catalytic performance of bulk and colloidal Co/Al layered double hydroxide with Au nanoparticles in aerobic olefin oxidation

Sónia R. Leandro,^a Cristina I. Fernandes,^a Ana S. Viana,^{a,b} Ana C. Mourato,^a Pedro D. Vaz,^c Carla D. Nunes^{a,b*} cmnunes@ciencias.ulisboa.pt

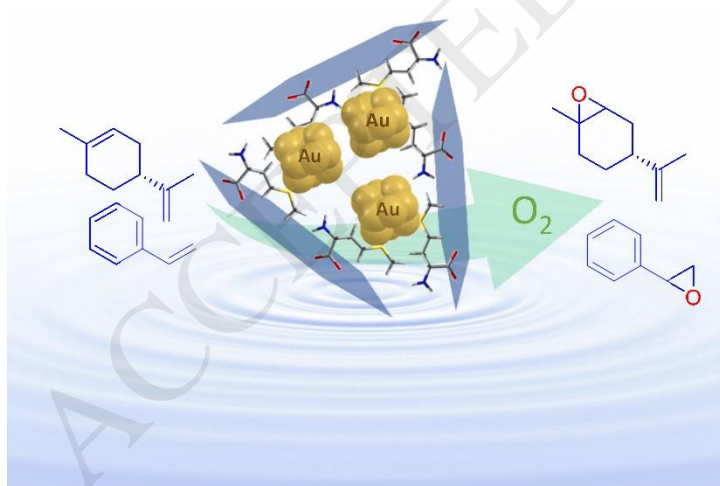
^a Centro de Química e Bioquímica, Faculdade de Ciências da Universidade de Lisboa, 1749-016 Lisboa, Portugal

^b Centro de Química Estrutural, Faculdade de Ciências e Instituto Superior Técnico, Universidade de Lisboa, 1049-001 Lisboa, Portugal

^c CICECO – Aveiro Institute of Materials, Department of Chemistry, University of Aveiro, 3810-193 Aveiro, Portugal

*Correspondence to: Dr. Carla D. Nunes Centro de Química e Bioquímica, Departamento de Química e Bioquímica, Faculdade de Ciências da Universidade de Lisboa, Campo Grande, Ed. C8, 1749-016 Lisboa, Portugal Centro de Química Estrutural, Faculdade de Ciências e Instituto Superior Técnico, Universidade de Lisboa, 1049-001 Lisboa, Portugal Tel: (+351) 217 500 216 Fax: (+351) 217 500 088

Graphical abstract



Co/Al hydrotalcite-Au nanoparticle catalysts show versatility for aerobic oxidation with high (stereo)selectivity.

Highlights

- Biomimetic Au nanoparticle synthesis yields active oxidation catalysts
- Exfoliated clays were very selective in aerobic olefin epoxidation
- Exfoliated catalysts showed higher stereoselectivity than bulk ones
- Exfoliated catalysts with higher catalytic potential than the bulk-based ones

ACCEPTED MANUSCRIPT

Abstract

A Co/Al layered double hydroxide material was synthesized in both bulk and exfoliated (colloidal) forms. Anion exchange with methionine allowed immobilization of Au nanoparticles previously prepared by a biomimetic method using an anti-oxidant tea aqueous extract to reduce the Au salt solution. The catalytic performance of bulk and exfoliated clays Au-hybrid materials was assessed in aerobic olefin epoxidation. Both catalysts were very active towards the epoxide products and with very interesting substrate conversion levels after 80 h reaction time. The Au-exfoliated material, where the nanosheets work as large ligands, yielded higher product stereoselectivity in the case of limonene epoxidation. This arises from a confined environment around the Au nanoparticles wrapped by the clay nanosheets modulating access to the catalytic active centres by reagents. Mechanistic assessment was also accomplished for styrene oxidation by DFT methods.

Keywords

Gold nanoparticles; Amino acids; Clays; Aerobic oxidation catalysis;

1. Introduction

Current environmental concerns are focused on the development of cheap catalysts leading to highly selective materials and therefore reducing by-products [1-3]. Such concerns aim at a lower consumption of natural resources as well as benign and impactless reaction media.

A large fraction of catalytic processes makes use of precious metals (second- and third-row transition metals). While still much unrivaled in terms of catalytic performance, these metals suffer from many drawbacks impacting negatively both industry and society [4].

On the other hand, Nature sustains its activity and offers an incredible range of materials relying on metals (Mg, Ca, Mn, Fe, Co, Ni, Cu, Zn, Al) that are typically cheaper, less toxic, and more benign than their heavier counterparts [4]. Exploring this rapidly, expanding new frontier in a field that is of importance for practical reasons (cost and availability, environmental impact, toxicity), will aim at the discovery of fundamentally new reactivity that can offer solutions to a broader range of catalytic problems. Understanding better the upgrading processes and developing viable alternatives will contribute to achieve new frontiers in catalysis [5].

To address the above concerns, clays and particularly layered double hydroxides (LDHs) are among the inorganic materials that have experienced a high development in recent years, owing to their applications in many fields, namely heterogeneous catalysis [6]. These materials are known for their ion exchange capacity, making possible the introduction of adequately functionalized guests. The importance of these materials is based on their ability to retain chemical species with electrical charges compatible to those of the layers. Concerning catalytic applications, the use of LDHs can still go much further in this field. The versatility of these materials goes beyond their ion exchange capacity, with tunable composition and form (powder, colloid, gel) [7-10]. The use of delaminated/exfoliated LDHs has been reported with several advantages, especially at the level of asymmetric synthesis [11]. This process makes possible to assess the LDHs as colloidal nanosheets that transform such materials in nanostructured catalysts. More recently, LDHs have been engineered as nanoparticles, as monoliths with hierarchical porosity, or as gelled nanoparticles with high concentration rendering in both cases such materials further new applications [9,10,12].

Increasing research in recent years led to new catalysts capable of carrying out reactions at lower temperatures and pressures with higher selectivity towards the desired products. Fostering new frontiers in reactivity and product selectivity this work aimed at exploring the chemistry of LDHs concerning its forms (bulk powder and delaminated) [7,10,11,13].

Concerning catalytic applications, the use of LDHs can still go much further in this field [14-22]. With this goal in mind we aim to develop new catalysts or catalyst forms towards more selective and efficient processes. In this work we present a study on the versatility of LDH-based catalysts

with Au nanoparticles. Au is known for its catalytic versatility in a variety of reactions. Although most of its applications is usually in aerobic oxidation of organic compounds (alkanes, olefins or alcohols) [23] the truth is that Au nanoparticles have found much more applications, including activation of oxygenated compounds, hydrogen transfer reduction or C–C coupling reactions [24]. In this work the versatility of these catalysts was explored under a multidimensional perspective. While LDHs can be prepared under different forms (bulk, exfoliated or gelled) we also explored their activity for their use as oxidation catalyst supports for Au nanoparticles, by tuning the reaction conditions and substrates. This work reports the use of Co/Al LDH materials that builds up on knowledge from previous research using Mg/Al LDH materials [13] to assess whether the composition of the host material influences catalytic performance. The outcome of this research is presented, discussed and benchmarked with other literature reports.

2. Experimental

2.1. General

All reagents and solvents were of analytical grade and bought from Sigma-Aldrich. In this work we have used *L*-methionine as the intercalating ligand and will be denoted as *met*. **HT_{Co/Al}-CO₃**, **HT_{Co/Al}-Cl**, and **HT_{Co/Al}-*met*** materials were synthesized by adopting a literature methodology [7]. ^{Ex}**HT_{Co/Al}-*met*** was exfoliated in formamide according to literature methods [7,13]. Au nanoparticles (**Au_{NP}**) were prepared adopting a biomimetic methodology described in the literature [25]. Detailed procedures can be found in the SI material.

2.2. Catalysts Preparation

HT_{Co/Al}-*met*-Au

Au_{NP} (17 mg) were added to a suspension of **HT_{Co/Al}-*met*** (700 mg) in deionized type II water. The resulting slurry was stirred under a N₂ atmosphere, at room temperature (303 K) for 12 h. The resulting materials were then filtered off, washed with deionized water (3x20 mL), and dried in a vacuum oven (313 K) for 48 h.

^{Ex}**HT_{Co/Al}-*met*-Au**

The ^{Ex}**HT_{Co/Al}-*met*** exfoliated material was used to prepare hybrid-sheet nanostructures with **Au_{NP}**. A given amount of the colloidal nanosheet material (15 ml, 0.10 mmol_{met}) was mixed with 4 mg of **Au_{NP}** (0.02 mmol_{Au}). The mixture was sonicated for 1 minute and then left stirring for 12 h at room temperature (303 K). The resulting colloid, denoted ^{Ex}**HT_{Co/Al}-*met*-Au**, had a different color (burgundy) due to the presence of the **Au_{NP}** and was found to be stable for a long time as well.

2.3. Catalytic epoxidation of olefins

Catalytic tests were carried out in a Carousel 12 Plus Reaction Station from Radleys. A given amount (1.6 mmol) of the olefin substrates – *cis*-cyclooctene, styrene, 1-octene, *trans*-2-hexen-1-ol, *R*-(+)-limonene – was mixed with dibutylether (1.6 mmol) (internal standard) and 15 μ L (5 mol %) of *tert*-butyl hydroperoxide (5.5 M solution in decane; *tbhp*). Then the catalyst was added to this mixture. This was either 10 mL of exfoliated materials ^{Ex}**HT**_{Co/Al}-*met*-**Au** (0.016 mol Au) with an extra 5 mL of acetonitrile or 100 mg of **HT**_{Co/Al}-*met*-**Au** (0.016 mol Au) bulk catalyst with 8 mL of toluene. The magnetically stirred mixture was heated to 353 K and kept for 80 h.

Substrate conversion and product yields were monitored by sampling at regular time intervals and analyzing it using a Shimadzu QP2100-Plus GC/MS system fitted with a capillary column (Teknokroma TRB-5MS or TRB-1MS).

All reactions started with *tbhp* acting as radical initiator with O₂ from air at atmospheric pressure being the oxidant. Control experiments were run in the presence of (a) N₂ inert atmosphere, and (b) in the presence of a radical scavenger (2,6-di-*tert*-butyl-4-methylphenol). This allowed confirming that O₂ was the oxidant and the existence of a radical reaction mechanism. The heterogeneous nature of the **HT**_{Co/Al}-*met*-**Au** catalyst was evaluated by analyzing its Au content by ICP-OES at the end of an oxidation reaction (*cis*-cyclooctene as substrate) and comparing it with the Au loading of the fresh catalyst.

3. Results and discussion

3.1. Catalysts characterization

Layered double hydroxides (LDH) are very versatile materials that can be prepared with organic anions by three major approaches: (i) anion exchange, (ii) coprecipitation and (iii) reconstruction [6]. In all these methods, when preparing LDHs with anions other than carbonate, contamination from CO₂ must be prevented, since the carbonate anion is readily incorporated and persistently held in the interlayer [6]. Therefore, decarbonated and deionized water with an inert atmosphere must be used to avoid exposure of the reacting material to air.

In this work we have used the coprecipitation method to prepare Co/Al LDH (denoted as **HT**_{Co/Al}) clay-based hybrid materials with *L*-methionine (*met*) as evidenced in Scheme 1 [7,13].

The synthesis provides the carbonate clay (**HT**_{Co/Al}-CO₃), which is then ion-exchanged with chloride anions to yield **HT**_{Co/Al}-Cl. The latter is easier to undergo further ion exchange (due to lower charge density of the Cl⁻ anion) to prepare organic-LDH materials. Introduction of *met* amino acid by ion exchanging the Cl⁻ anions was carried out by a literature protocol [13], yielding

HT_{Co/Al}-met material. Based on the *S*-content from elemental analysis, the amino acid loading was 1.82 mmol·g⁻¹. According to the empirical formula expected for the **HT_{Co/Al}** material – [Co₆Al₂(OH)₁₆](Cl)₂·4H₂O – the intercalated **HT_{Co/Al}-met** clay can be rationalized as [Co₆Al₂(OH)₁₆](met)_{1.11}(Cl)_{0.89}·4.6H₂O with the water content being estimated from thermogravimetric analysis, as will be discussed later in this work.

Reaction of **HT_{Co/Al}-met** with gold nanoparticles (**Au_{NP}**) afforded the new **HT_{Co/Al}-met-Au** hybrid material and the Au loading was found to be 1.16 wt.-% corresponding to 5.9×10⁻² mmol_{Au}·g⁻¹ for this material.

The amino acid containing clay **HT_{Co/Al}-met** synthesized previously was also subjected to an exfoliation procedure to prepare 2D mixed-metal inorganic nanosheet materials modified with the *L*-containing amino-acid. This step yielded a deep pink colloidal formamide solution of the clay denoted as ^{Ex}**HT_{Co/Al}-met**. The choice of this amino acid to conduct exfoliation was found to be quite adequate given that the colloids were found to be stable for at least 24 months. This matches other reports found in the literature addressing the exfoliation of LDH materials with larger anions (such as sodium dodecyl sulfate) [6,7].

[Scheme 1 here]

Thermogravimetric analysis (TGA) also confirmed the intercalation of *met* in the interlayer spacing of the HT LDH material. According to Figure 1, *met* abruptly decomposes at temperatures in the 500 – 650 K range. After this range, decomposition carries till ca. 3.2% at 1073 K, but at slower pace.

In the case of **HT_{Co/Al}-met** its thermal profile evidences a mass loss of 12% till ca. 493 K, which may be due to water (both adsorbed and intercalated). The material then further decomposes in a two-step way till 1073K, accounting for a total of 27% of the initial weight. Assuming this to arise exclusively from decomposition of methionine, this yields a loading of 1.82 mmol·g⁻¹ in the **HT_{Co/Al}-met** material. This shows an excellent agreement with results from elemental analysis (discussed above). Caution should however prevail, as at higher temperature some dehydroxilation is likely to occur and therefore the real content of methionine may be slightly lower [13]. The decomposition profile should be commented as well; in this case the profile is different from that observed for neat *met*, which can be a proof that *met* is indeed intercalated within the interlayer spacing of the HT host and is therefore protected against thermal decomposition due to specific host-guest interactions [26].

Electronic spectroscopy (using both absorption and diffuse reflectance techniques) was used to assess formation on the Au-containing hybrid materials. For both materials containing the Au_{NP} , $\text{HT}_{\text{Co/Al-}met\text{-Au}}$ and $^{\text{Ex}}\text{HT}_{\text{Co/Al-}met\text{-Au}}$, the measured spectra are shown in Figure 2.

The measured spectra show that both $\text{HT}_{\text{Co/Al-}met\text{-Au}}$ and $^{\text{Ex}}\text{HT}_{\text{Co/Al-}met\text{-Au}}$ materials displayed the surface plasmon resonance band at wavelengths similar to those observed for the as-synthesized gold nanoparticles (Au_{NP}), indicating the successful formation of the hybrid materials [13]. In addition, changes at the measured absorbance maxima of the hybrid materials also evidence that there may be interaction between the Au_{NP} and the host $\text{HT}_{\text{Co/Al-}met}$ and $^{\text{Ex}}\text{HT}_{\text{Co/Al-}met}$ materials [13]. This is most evident for the absorbance maxima of the exfoliated $^{\text{Ex}}\text{HT}_{\text{Co/Al-}met\text{-Au}}$ material, where not only the surface plasmon resonance band shifted (to 558 nm) but also the methionine bands experienced shifts. In this case the bands from methionine (631 and 671 nm for the neat compound) shifted to 610 and 656 nm, respectively, indicating that the interaction between Au_{NP} and methionine is stronger than that found for the bulk $\text{HT}_{\text{Co/Al-}met\text{-Au}}$ material, where the shifts were smaller.

The morphology and size of the exfoliated nanosheets in $^{\text{Ex}}\text{HT}_{\text{Co/Al-}met}$ were examined by TEM, as shown in Figure 3.

As shown in Figure 3a for $^{\text{Ex}}\text{HT}_{\text{Co/Al-}met}$, the TEM image of this material shows an assembly of thin sheets with homogeneous contrast, reflecting their ultrathin nature and uniform thickness [7,13], also supported by AFM as discussed in the following lines. The diffraction pattern (inset in Figure 3a) shows a hexagonal arrangement agreeing with that expected for these materials [7]. On the other hand, Figure 3b shows the interaction between Au_{NP} and the exfoliated sheets the success of the assembly in $^{\text{Ex}}\text{HT}_{\text{Co/Al-}met\text{-Au}}$. This image shows clearly the presence of the LDH exfoliated thin sheets of $^{\text{Ex}}\text{HT}_{\text{Co/Al-}met}$ (grey areas) along with the geometric shapes (dark spots with pyramid, hexagon, etc... shapes) typical from Au_{NP} structures.

AFM imaging of exfoliated nanosheets was also carried out, as illustrated in Figure 4, to have additional information on their morphology and thickness before and after interaction with Au_{NP} . Typically, larger $^{\text{Ex}}\text{HT}_{\text{Co/Al-}met}$ nanosheets exhibited a thickness of ca. 4 nm (Figure 4a pointing to the presence of multilamellar nanosheets [7]). Upon the formation of the hybrid materials $^{\text{Ex}}\text{HT}_{\text{Co/Al-}met\text{-Au}}$ (Figure 4b), individual gold nanoparticles and small nanoclusters are clearly depicted over the clay nanosheets, conferring a more heterogenous morphology. Nevertheless, the $^{\text{Ex}}\text{HT}_{\text{Co/Al-}met\text{-Au}}$ nanosheets profile reveals that overall thickness, comparing profile data from both $^{\text{Ex}}\text{HT}_{\text{Co/Al-}}$

met and ^{Ex}**HT**_{Co/Al}-*met*-**Au** materials was maintained (ca. 4 nm in Figures 4a and 4b), highlighting the stability of methionine interlayer.

Figure 5 shows the powder XRD patterns of the nanohybrid materials **HT**_{Co/Al}-*met* and **HT**_{Co/Al}-*met*-**Au**. These materials display a series of well-developed Bragg reflections in the 2θ range 4° - 70° , which can be indexed to the hexagonal layered LDH structure with rhombohedral symmetry [27,28]. This also agrees with the electron diffraction pattern from the TEM measurements (discussed above). No peaks of impurities were discerned, indicating the high purity of the product.

Several intense peaks due to basal reflections (001) at low 2θ angles allowed us to estimate directly the normal basal spacing to the plane (001) which is equal to the thickness of one lamella of the brucite structure (ca. 4.8 Å) plus the thickness of the interlayer region [29]. To calculate this the second 2θ value was used corresponding to plane (003). In the case of the **HT**_{Co/Al}-*met* parent material the 003 reflection was located at a 2θ value of 5.8° , corresponding to an interlayer spacing of 10.4 Å, after subtracting the brucite layer thickness (ca. 4.8 Å). This indicates that the *met* amino acid adopted a tilted vertical arrangement between the lamella [30,31]. Caution should prevail in this analysis as the interlayer arrangement depends on many other factors (e.g. hydration level and temperature conditions), which were not accounted for in this estimation.

In addition, peaks due to the presence of the **Au**_{NP} structures were identified at $2\theta = 38.2^\circ$, 44.4° and 64.6° (Figure 3, arrow markers). The average size of the **Au**_{NP} structures according to the Debye-Scherrer equation and based on data from the peak at $2\theta = 38.2^\circ$ was estimated to be 31 nm. This value agrees well with the size found for those structures based on the AFM measurements, 40 nm, and TEM images (average size found was 29 nm). Such size magnitude would render the **Au**_{NP} structures as inactive for catalytic applications. However, according to Figure 3 (TEM images), a closer look at the bottom image shows that there is a size distribution for the **Au**_{NP} structures. Sizes varied between ca. 4 and 70 nm with ca. 56% of the nanoparticles to fall between 4 and 24 nm, according to the method we followed [32]. Such size distribution agrees with the observed color, rendering potential catalytic activity (which is known to be favored for smaller nanoparticles) as will be discussed later in this work. In this case, we observed that the rough control of the size and shape of the nanoparticles is advantageous for the observed catalytic activity. Given that the scope of the manuscript is also on taking advantage on the biomimetic synthesis method of the nanoparticles, we think this is a feature of this approach, although we are aware that the Au nanoparticles size is far from optimum.

Diffuse reflectance infrared spectroscopy (DRIFT) was used to characterize the hybrid materials, shown in Figure 6.

The FTIR spectra of **HT_{Co/Al}-Cl**, **HT_{Co/Al}-met** and **HT_{Co/Al}-met-Au** (Figure 6a) show similar profiles. They present strong bands at 1360-1400 cm⁻¹ and 810 cm⁻¹, corresponding to the stretching and deformation modes of CO₃²⁻. All materials showed a band centered at ca. 3440 cm⁻¹ being assigned to the νO-H mode of hydroxyl groups, while the presence of a shoulder at ca. 3150 cm⁻¹ suggests that water molecules are interacting with other species by hydrogen bonding. The remaining bands observed below 800 cm⁻¹ may be associated with bonds between metals and oxygen atoms in the structure of the clay [13]. According to the spectrum of the material containing the methionine amino acid, **HT_{Co/Al}-met**, it was possible to assign bands to the νC-H, νC-O and νC=O modes of the amino acid moiety (Figure 6b).

Bands corresponding to νN-H vibrational modes, expected in the 3300-3500 cm⁻¹ range could not be observed due to overlapping. By the same token, νC-N modes, expected between 1020-1220 cm⁻¹ were not observed due to overlap of the νC-O modes. The characteristic band of the binding of the metals of the lamella hydroxyl, νM-O modes, appears in the form of a broad band around 600 cm⁻¹.

3.2. Catalytic studies on epoxidation of olefins

The synthesized nanohybrid clay materials **HT_{Co/Al}-met-Au** and **^{Ex}HT_{Co/Al}-met-Au** were tested as catalysts for epoxidation of olefins. The test-set comprised *cis*-cyclooctene, 1-octene, *trans*-hex-2-en-1-ol, *R*-(+)-limonene and styrene as substrates. All reactions were carried out using *tert*-butyl hydroperoxide (tbhp in decane) as the initiator (5 mol%), under aerobic conditions (molecular O₂ as the oxidant) and run at 353 K, with results gathered in Table 1. Control runs (without catalyst and in the presence of tbhp and O₂) gave virtually no conversion of starting material at 353 K. The materials without Au, **HT_{Co/Al}-met** and **^{Ex}HT_{Co/Al}-met**, were also tested for their intrinsic catalytic activity and to assess their influence in the results. The results showed that both materials had a catalytic activity with average cyclooctene conversion below 5% after 80 h.

The oxidation of *cis*-cyclooctene using **HT_{Co/Al}-met-Au** and **^{Ex}HT_{Co/Al}-met-Au** materials as catalysts (Table 1) displayed very good to excellent substrate conversion after 80 h of reaction (lowest value was 74% for **^{Ex}HT_{Co/Al}-met-Au**). The observed selectivity values towards the epoxide followed the same trend (above 90%), but not “100%”, which is expected for radical-based mechanisms due to side-reactions, as recently described by us [13]. The by-products found in the reaction were both the enone and enol being detected with selectivity below 5% (Table 1, entries 1

and 5). The results obtained for cyclooctene are in line with those reported for the same substrate using Au or Ag nanoparticles [33,34]. Bawaked and coworkers, reported that cyclooctene oxide was obtained with ca. 80% selectivity, while Chen described that cyclooctene was oxidized to its epoxide with a selectivity of 97%, being in both cases similar to that reported in the present work (above 90%).

To confirm the radical nature of the reaction we conducted *cis*-cyclooctene oxidation in the presence of a radical trap (2,6-di-*tert*-butyl-4-methylphenol). In this case we observed very low substrate conversion (< 5%) being consistent with the fact that free radicals are active species in the catalytic cycle, agreeing with other reports for related systems [13,33,34]. The heterogeneous nature of the **HT_{Co/Al}-met-Au** catalyst concerning gold nanoparticle's (**Au_{NP}**) leaching was also evaluated. After a *cis*-cyclooctene oxidation experiment finished, the catalyst was separated by filtration from the reaction slurry and analyzed by ICP. Results showed that the Au loading was found to be 1.07 wt.-%. Compared to the Au loading in the fresh catalyst (1.16 wt.-%) showing a leaching of 8%, confirming that the **HT_{Co/Al}-met-Au** catalyst is truly heterogeneous.

Both catalysts were then further studied for their activity using other substrates such as 1-octene, *trans*-hex-2-en-1-ol and *R*-(+)-limonene. This set of olefins yielded different results from the previous one, with the oxidation of 1-octene being the lowest performing system. 1-octene is an unbranched terminal olefin presenting low reactivity, similarly to other reports found in the literature [13]. According to Table 1, **HT_{Co/Al}-met-Au** catalyst made possible to achieve 32% substrate conversion, while the exfoliated counterpart did not show any activity at all with this substrate (Table 1, entry 6). For the case of the bulk catalyst the major product was found to be 2-Hexyloxirane with 85% selectivity with octan-2-one being the by-product. Oxidation of the *trans*-hex-2-en-1-ol allylic alcohol evidenced lower substrate conversion when the exfoliated catalyst was used, compared to the performance of the bulk counterpart (Table 1, entries 3 and 7). In addition, striking differences on product selectivity were found between both catalytic systems. While the bulk **HT_{Co/Al}-met-Au** catalyst showed an epoxide selectivity of 97% at the end of the reaction (80 h), the exfoliated one yielded the same product with a selectivity of only 64%. In both cases, the by-product formed was the α,β -unsaturated aldehyde (Table 1, entries 4 and 8). Formation of the α,β -unsaturated aldehyde has been reported in the literature for a set of allylic alcohols using **Au_{NP}** supported on CeO₂ [35]. However, authors also noticed that when the catalyst changed to mixed Au(Pd) nanoparticles supported on TiO₂, the aldehyde was not the major product due to competing catalytic processes. In the present case, we did not observe such high activity as in that case and the product selectivity was different with the epoxide being the major product.

The oxidation of *R*-(+)-limonene followed a different trend from that observed for the allylic alcohol described above. As shown in Figure 7, both catalysts achieved a very good level of substrate conversion (above 74% after 80 h, according to Table 1). In addition, product selectivity was found to follow the same trend for both catalysts, with carvone (the enone product) being the major product (Table 2 and Figure 7). Moreover, for both catalysts the minor product was found to be the endocyclic epoxide and carveol (the enol product) was never detected.

Despite this, the most striking feature was the *cis/trans* diastereomeric ratio evidenced by both catalyst, which differed completely (Figure 7)

That was an outstanding feature distinguishing it from the bulk counterpart. According to Figure 7, while the bulk catalyst yielded the epoxide without a clear preference for any of the diastereomers, the exfoliated one originated mostly the *cis* diastereomer of the endocyclic epoxide (Table 1, entry 8) with a trend for slight increase with time (Figure 7c). That was a remarkable achievement following the same trend as described in the literature [11,13]. As recently demonstrated by us, the main reason for this, may arise from the fact that the LDH nanosheets with the chiral amino-acids work as large ligands around the **Au**_{NP}. This consequently constrains the way reactants interact with active sites [11,13]. The higher *cis/trans* diastereomeric ratio observed with the exfoliated catalyst (Figure 7c) also demonstrates that in this case the same effect was observed concerning the stereocontrol of the process by constraining how reactants reach the active sites [11,13].

This can be explained by the structural differences of both catalysts. According to Scheme 2, while in the bulk catalyst the **Au**_{NP} structures are outside the LDH particles, in the bulk they are wrapped by the exfoliated LDH nanosheets. This results in the fact that the bulk catalyst provided better access of the substrates to the active centers, whereas for the exfoliated one there must be some diffusion process of substrates through the exfoliated nanosheets till the active centers are reached. The outcome was the observation of higher substrate conversion (except for limonene) for the bulk catalyst. Additionally, this diffusion feature of the exfoliated catalyst is also responsible for the observed enhanced diastereoselectivity in limonene oxidation (as evidenced in Figure 7), since the substrate approach is constrained as already discussed above.

As mentioned earlier in this work, the observed selectivity values for epoxide products were generally high. It could however be anticipated, as it would be expected for radical-based mechanisms due to side-reactions being supported by mechanistic proposals found in the literature.

We have tested another substrate – styrene – which differs from the previously described since it lacks H-atoms in α -position to the olefin moiety and, therefore, it is likely to follow a slightly different mechanism [13,33,36].

Oxidation of styrene usually yields a set of economically valuable products: the epoxide, benzaldehyde and benzoic acid. While the latter was never observed in the tests carried out using any of the catalysts, the remaining two were found to be produced in different ratios depending on the catalyst used. According to Table 2, both catalysts performed quite well, with the bulk one being more active concerning substrate conversion.

The reaction kinetics on the substrate conversion was found to be overlapping for the first 8 h of reaction without distinguishing features for any of the catalysts, as evidenced in Figure 8. Another interesting feature was the fact that when the reactions were run with catalyst but under N_2 atmosphere slower kinetics were observed confirming O_2 as a key-factor to feed the process, as evidenced in Figure 8a. Concerning product selectivity, benzaldehyde was found to be the major product when the **HT_{Co/Al-met-Au}** bulk catalyst was used. On the other hand, when **^{Ex}HT_{Co/Al-met-Au}** was the catalyst, styrene oxide was the main product formed. Another interesting feature was the fact that acetophenone was detected (in very low yield) when the bulk catalyst was used, but surprisingly it was not detected when using the exfoliated catalyst. All these facts are shown in Figure 8. This product selectivity tuning between both catalysts may arise from different surface characteristics. According to Scheme 2, there are expected differences for the **Au_{NP}** structures, which are more exposed to the reaction medium in the **HT_{Co/Al-met-Au}** bulk catalyst and not so much in the **^{Ex}HT_{Co/Al-met-Au}** one. This will result in different interaction levels between the reactive species and surfaces, which may result in product selectivity tuning [37].

The presence of phenylacetaldehyde was reported in the literature, but not observed in this study [13,33,34]. Acetophenone (**Acph**, Scheme 3) was detected instead (Table 2, entry 2). According to the literature, phenylacetaldehyde may arise from an isomerization of the epoxide after opening the oxyrane ring. In the present work, we believe that acetophenone may be formed by the same process with the oxyrane ring opening in the “opposite direction” to that required to form phenylacetaldehyde (**Phac**), as shown in Scheme 3. Oxidation of styrene to acetophenone has been reported in the literature [38]. When using Au nanoparticles, benzaldehyde was the major product, but when Pd was used in combination with Au, acetophenone was the major product [38].

The above proposal demonstrates how the radical mechanism may progress as styrene lacks the presence of H-atoms in α -position to the olefin moiety, which would make impossible to rationalize H-atom abstraction [34,36]. Alternatively, styrene recombines directly with tbhp radicals yielding a couple of intermediaries (**1** and **2** in Scheme 3). These will then decompose to yield either styrene oxide or benzaldehyde, depending on the path followed (Scheme 3). The *t*-butyl derivative radicals will recombine (or not) with O₂ closing and feeding the catalytic cycle [36].

This mechanistic proposal prompted us to further explore this deeper making use of Density Functional Theory (DFT) calculations applied on the intermediaries mentioned above to assess the associated thermodynamics. All calculations were performed exclusively for the energetics of the reagents and products without accounting for the catalyst's influence.

In this way, the very first step should be the initiation step with decomposition of tbhp to yield the initiator radicals **TB1** and **TB2**, according to Scheme 3. Following this, radical **TB1** will react with styrene (**S**) yielding intermediary **1** (Figure 9). The reaction is endergonic with a calculated ΔG of 23.2 kcal mol⁻¹ in acetonitrile (23.5 kcal mol⁻¹ in toluene). Intermediary **1** will consequently decompose straightforward towards formation of the epoxide (**E**) and radical **TB**. The reaction in this case is exergonic with a calculated ΔG of -24.7 kcal mol⁻¹ in acetonitrile (-24.6 kcal mol⁻¹ in toluene).

On the other hand, concomitantly, radical **TB2** can also react with styrene (**S**) to yield intermediary **2** (Figure 10). This reaction is endergonic (similarly to the formation of intermediary **1**) with a calculated ΔG of 19.5 kcal mol⁻¹ in acetonitrile (19.8 kcal mol⁻¹ in toluene). According to Scheme 3, decomposition of intermediary **2** is more challenging than that of **1**. Peroxide **2** decomposes through two possible pathways (Figure 10).

It can yield the epoxide **E** and radical **TB1** (which will feed the cycle, Scheme 3) or di-radical **3** by loss of **TB** radical. According to DFT results both paths are exergonic. Decomposition of **2** towards **E** is predicted to have a calculated ΔG of -13.6 kcal mol⁻¹ in acetonitrile (-13.7 kcal mol⁻¹ in toluene), while decomposition towards **3** will have a calculated ΔG of -35.8 kcal mol⁻¹ in acetonitrile (-36.0 kcal mol⁻¹ in toluene). Further decomposition of intermediary **3** yielding formaldehyde and benzaldehyde is predicted to be slightly endergonic with a ΔG of only 3.2 kcal mol⁻¹ in acetonitrile (3.1 kcal mol⁻¹ in toluene), according to Figure 11a.

This confirms that, although likely to occur, the isomerization step is not a favored pathway with these catalysts, being a relevant differing feature of these catalysts compared to others found in the literature [34,36].

On the other hand, the likely formation of phenylacetaldehyde (**Phac**) and/or acetophenone (**Acph**) arising from an isomerization step on the epoxide E, is also predicted to be slightly exergonic as evidenced in Figure 11b, which accounts for the low yield of these products. It is worth remembering that in this work only acetophenone was obtained and exclusively when the catalyst was **HT_{Co/Al}-met-Au** (Figure 8).

Regeneration of **TB** radical by reaction with O₂ (yielding **TB2**) is an endergonic process with a calculated ΔG of 37.5 kcal mol⁻¹ in acetonitrile (32.1 kcal mol⁻¹ in toluene) as shown in Figure 11c. From the results discussed above, the steps involving the reaction of radicals **TB1** and **TB2** with styrene (**S**), as well as the regeneration reaction of radical **TB** with O₂ may account for an induction period observed experimentally at early stages of the reaction, given that these reactions have free energy barriers in the 20-40 kcal mol⁻¹ range at 353 K.

4. Conclusions

Continuing our efforts to prepare sustainable and environmentally friendly catalysts we reported in this work a set of clay-based catalysts with Au nanoparticles. Their activity was tested in olefin oxidation catalysis. The set of clay materials covered both bulk and exfoliated (colloid) versions, while the Au nanoparticles were synthesized using tea extract with a high load of antioxidants. This was also a sustainable water-based biomimetic procedure.

The catalysts were highly selective towards the epoxide products. Substrate conversion was also found to be generally very high (above 74%, Table 1) with the exception being the oxidation of 1-octene. In this case, the bulk catalyst, achieved 32% substrate conversion, while the exfoliated counterpart did not show any activity at all. This could be expected for this compound as it is an unbranched terminal olefin.

By the same token the bulk catalyst evidenced higher activity than the colloidal catalyst for *cis*-cyclooctene and *trans*-hex-2-en-1-ol. For *cis*-cyclooctene, both catalysts yielded the corresponding epoxide almost exclusively, but for the allylic alcohol epoxide selectivity was always high, since it was found to be dependent on the catalyst form.

Stereoselectivity increased when using the exfoliated catalysts, as demonstrated in the epoxidation of limonene, where the synergy of a chiral ligand together with the clay nanosheets seems to play a definitive role. (see Figures S1 and S2 in SI material).

Styrene oxidation has shown similar differences. While the bulk catalyst evidenced higher substrate conversion, but lower epoxide selectivity (and a third product). The exfoliated one showed lower

conversion but almost twice epoxide selectivity, showing that the choice of the catalyst form is relevant.

The mechanistic proposal for styrene oxidation based on DFT calculations, also showed that the regeneration of the *tert*-butyl radical (**TB** yielding **TB2**) may be responsible for the rate determining step, in addition to formation of intermediaries **1** and **2** (Scheme 3).

This renders excellent perspectives for future developments of this system, which are being endeavoured by us.

Acknowledgments

The authors would like to acknowledge FCT for financial support (project UID/MULTI/00612/2013). CIF (SFRH/BD/81029/2011) and AM (SFRH/BPD/35036/2007) also acknowledge FCT for financial support. G09 calculations were made possible due to the computing resources provided by STFC Scientific Computing Department's SCARF cluster. We also thank the reviewers for raising pertinent questions that contributed largely to improve this manuscript.

References

- 1 D. Astruc, Nanoparticles and catalysis, Wiley- VCH Verlag GmbH & Co. KGaA, 2008.
- 2 R.J. White, R. Luque, V.L. Budarin, J.H. Clark, D.J. Macquarrie, Chem. Soc. Rev. 38 (2009) 481–494.
- 3 L. Mai, F. Yang, Y. Zhao, X. Xu, L. Xu, B. Hu, Y. Luo, H. Liu, Mater. Today 14 (2011) 346–353.
- 4 European Cluster on Catalysis, www.catalysiscluster.eu, (accessed July 2019).
- 5 SPIRE, www.spire2030.eu/sites/default/files/pressoffice/spire-roadmap.pdf, (accessed July 2019).
- 6 C.I. Fernandes, C.D. Nunes, P.D. Vaz, Curr. Org. Synth. 9 (2012) 670–694.
- 7 Z. Liu, R. Ma, M. Osada, N. Iyi, Y. Ebina, K. Takada, T. Sasaki, J. Am. Chem. Soc. 128 (2006) 4872–4880.
- 8 Y. Tokudome, N. Tarutani, K. Nakanishib, M. Takahashia, J. Mater. Chem. A 1 (2013) 7702–7708.
- 9 N. Tarutani, Y. Tokudome, M. Fukui, K. Nakanishi, M. Takahashi, RSC Adv., 2015, 5, 57187–57192.
- 10 Y. Tokudome, T. Morimoto, N. Tarutani, P.D. Vaz, C.D. Nunes, V. Prevot, G.B.G. Stenning, M. Takahashi, ACS Nano 10 (2016) 5550–5559.
- 11 J. Wang, L. Zhao, H. Shi, J. He, Angew. Chem. Int. Ed. 50 (2011) 9171–9176.

- 12 D. Kino, Y. Tokudome, P.D. Vaz, C.D. Nunes, M. Takahashi, J. Asian Ceramic Socs. 5 (2017) 466–471.
- 13 S.R. Leandro, A. Mourato, U. Łapińska, O.C. Monteiro, C.I. Fernandes, C.D. Nunes, P.D. Vaz, J. Catal. 358 (2018) 187–198.
- 14 L. Li, L. Dou, H. Zhang, Nanoscale 6 (2014) 3753–3763.
- 15 L. Wang, J. Zhang, X. Meng, D. Zheng, F. Xiao, Catal. Today 175 (2011) 404–410.
- 16 J. Wang, X. Lang, B. Zhaorigetu, M. Jia, J. Wang, X. Guo, J. Zhao, ChemCatChem 6 (2014) 1737–1747.
- 17 X. Wang, G. Wu, F. Wang, K. Ding, F. Zhang, X. Liu, Y. Xue, Catal. Commun. 28 (2012) 73–76.
- 18 S. Nakagaki, M. Halma, A. Bail, G.G.C. Arizaga, F. Wypych, J. Colloid Interf. Sci. 281 (2005) 417–423.
- 19 X. Bai, Y. Gao, H. Liu, L. Zheng, J. Phys. Chem. C 113 (2009) 17730–17736.
- 20 F. Lin, R. Doong, J. Phys. Chem. C 115 (2011) 6591–6598.
- 21 K. Layek, M.L. Kantam, M. Shirai, D. Nishio-Hamane, T. Sasaki, H. Maheswaran, Green Chem. 14 (2012) 3164–3174.
- 22 H.K. Kadam, S G. Tilve, RSC Adv. 5 (2015) 83391–83407.
- 23 A. Corma, H. Garcia, Chem. Soc. Rev. 37 (2008) 2096–2126.
- 24 M. Stratakis, H. Garcia, Chem. Rev. 112 (2012) 4469–4506.
- 25 D. Cruz, P.L. Falé, A. Mourato, P.D. Vaz, M.L. Serralheiro, A.R.L. Lino, Colloids and Surf. B: Biointerf. 81 (2010) 67–73.
- 26 I.J. Marques, P.D. Vaz, A.C. Fernandes, C.D. Nunes, Microporous Mesoporous Mater. 183 (2014) 192–200.
- 27 C. Taviot-Gueho, F. Leroux, C. Payen, J.P. Besse, Appl. Clay Sci. 28 (2005) 111–120.
- 28 H.-J. Kim, K. Ryu, J.-H. Kang, A.-J. Choi, T. Kim, J.-M. Oh, Sci World J. (2013) 421967.
- 29 J.C. Dupin, H. Martinez, C. Guimon, E. Dumitriu, I. Fechete, Appl. Clay Sci. 27 (2004) 95–106.
- 30 P.D. Vaz, C.D. Nunes, New J. Chem. 34 (2010) 541-546.
- 31 M. Vasconcellos-Dias, C.D. Nunes, P.D. Vaz, P. Ferreira, M.J. Calhorda, Eur. J. Inorg. Chem. (2007) 2917-2925.
- 32 A.A. Giro Dos Santos, Biossíntese, caracterização e citotoxicidade de nanopartículas de ouro usando extracto de lúcia-lima e erva de São Roberto (<http://hdl.handle.net/10451/4136>), MSc thesis, Universidade de Lisboa, Lisboa, 2010.
- 33 S. Bawaked, N.F. Dummer, D. Betchell, D.W. Knight, G.J. Hutchings, Green Chem. 13 (2011) 127–134.

34 Z. Chen, R.L. Luck, *Green Chem.* 18 (2016) 3354–3359.

35 A. Abad, A. Corma, H. García, *Pure Appl. Chem.* 79 (2007) 1847–1854.

36 P. Cancino, V. Paredes-García, P. Aguirre, E. Spodine, *Catal. Sci. Technol.* 4 (2014) 2599–2607.

37 A.S. Alshammari, *Catalysts* 9 (2019) 402.

38 X. Wang, N.S. Venkataramanan, H. Kawanami, Y. Ikushima, *Green Chem.* 9 (2007) 1352–1355.

ACCEPTED MANUSCRIPT

Figures

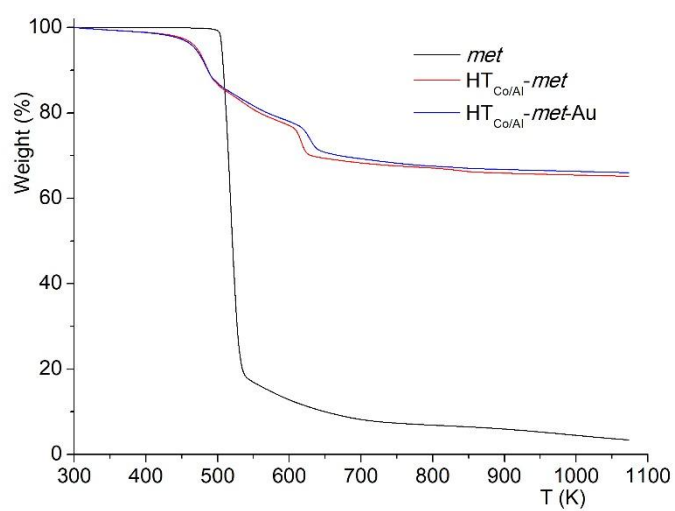


Figure 1. TGA profiles obtained under N₂ atmosphere at 10 K/min of *met*, HT_{Co/Al}-*met* and HT_{Co/Al}-*met*-Au.

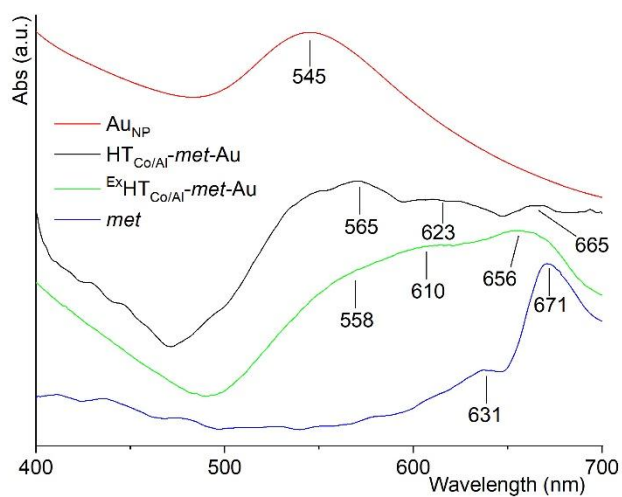


Figure 2. Electronic spectra of gold nanoparticles (Au_{NP}), methionine (*met*), and of the hybrid clay materials $\text{HT}_{\text{Co/Al}}\text{-met-Au}$ and $\text{HT}_{\text{Co/Al}}\text{-met-Au}$. The spectra of the hybrid materials were obtained as diffuse reflectance (DRUV) while the remaining were obtained from aqueous solutions in transmission.

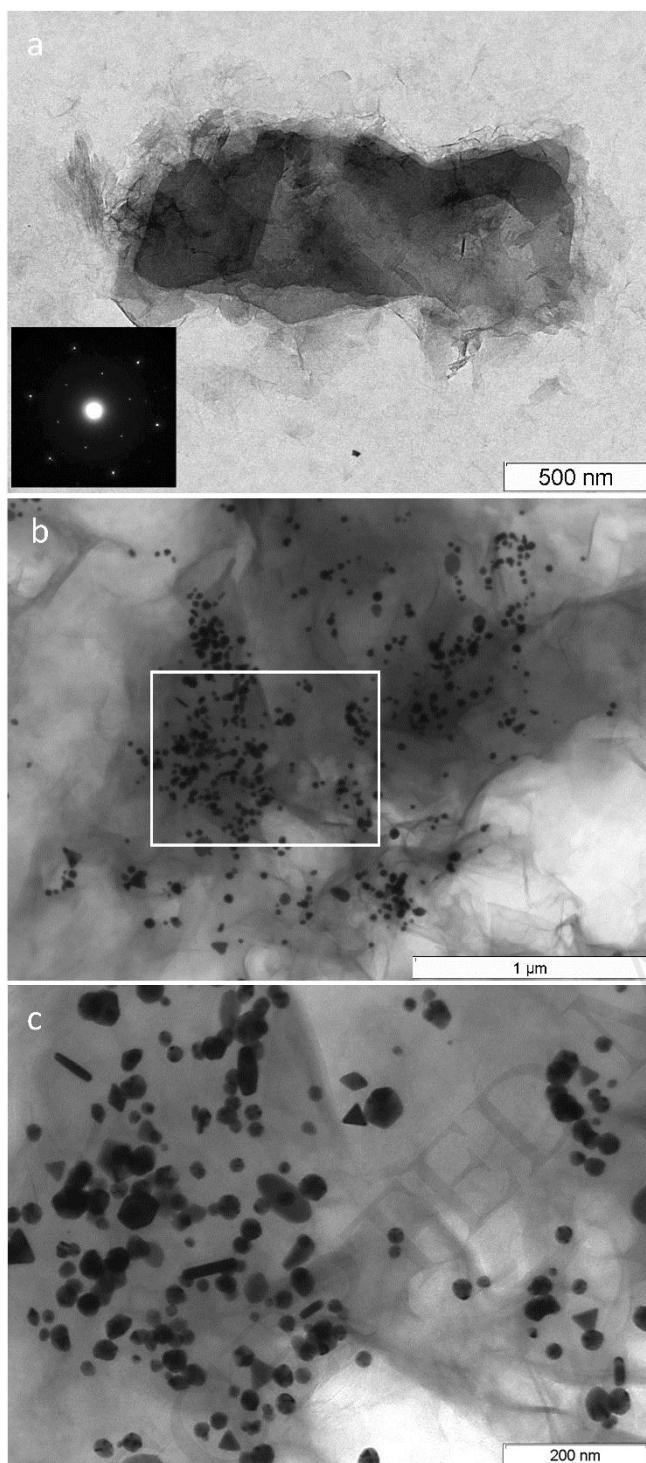


Figure 3. TEM images of $\text{ExHT}_{\text{Co/Al}}\text{-met}$ (a) and $\text{ExHT}_{\text{Co/Al}}\text{-met-Au}$ (b). The inset in the top image displays the diffraction pattern of the sample and evidences a hexagonal symmetry expected for these samples. In the middle image (b) one can see the Au_{NP} wrapped with the sheets of $\text{ExHT}_{\text{Co/Al}}\text{-met}$, while image (c) is a zoom of the area highlighted in image (b).

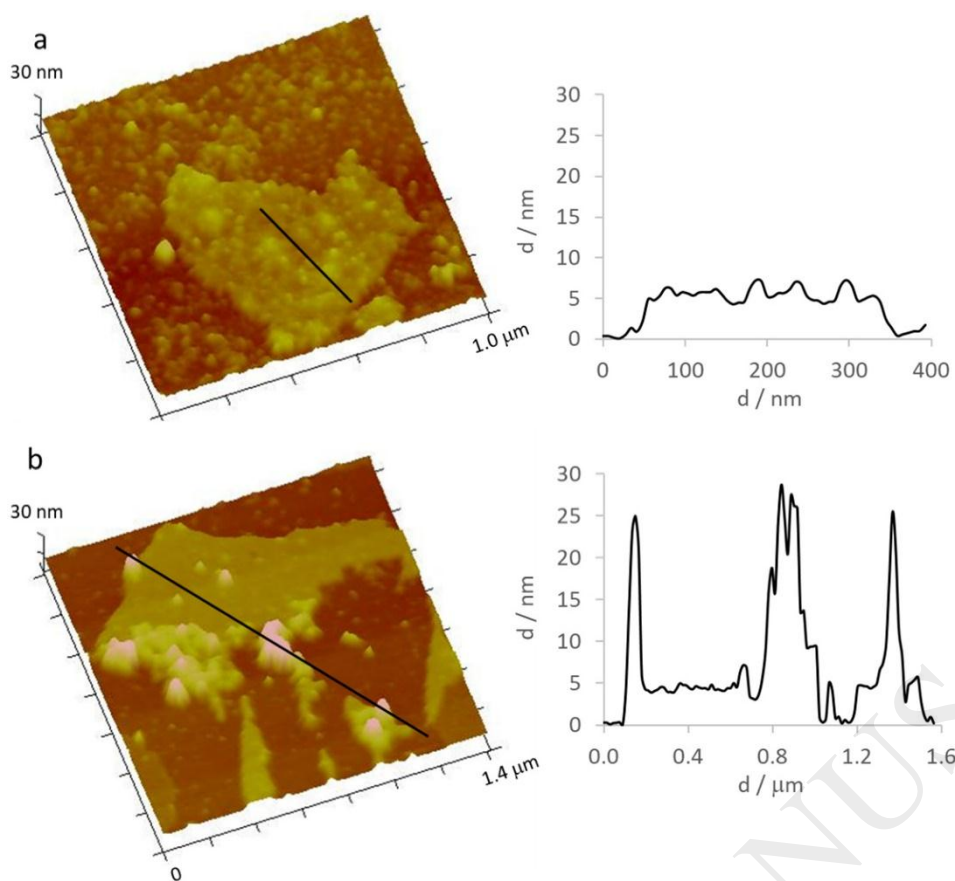


Figure 4. 3D AFM images of $ExHT_{Co/Al-met}$ (a) and $ExHT_{Co/Al-met-Au}$ (b) and corresponding profiles.

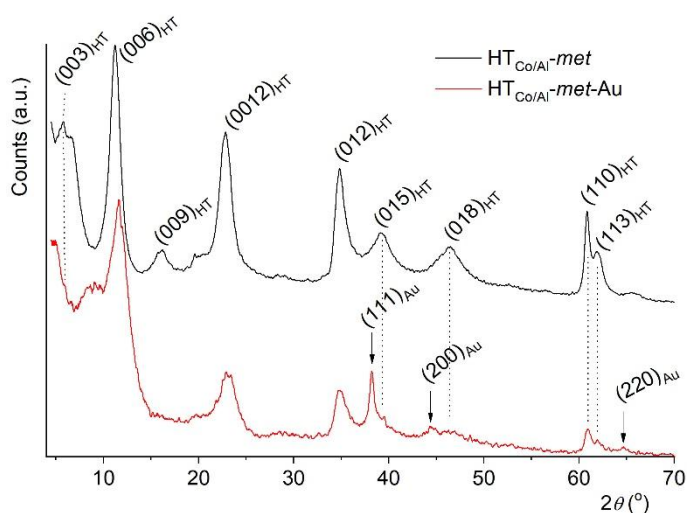


Figure 5. XRD powder patterns of $\text{HT}_{\text{Co/Al-met}}$ and $\text{HT}_{\text{Co/Al-met-Au}}$. The peak at $2\theta = 5.74^\circ$ is assigned to the 003 peak corresponding to the interlayer space containing the methionine guests. Diffraction peaks arising from Au_{NP} in HT-met-Au are highlighted with an arrow at $2\theta = 38.2^\circ$, 44.4° and 64.6° while the dotted lines next to it are eye-guides to mark the position of the diffraction peaks arising from the clay. Diffraction peak indexation was based on literature data [28].

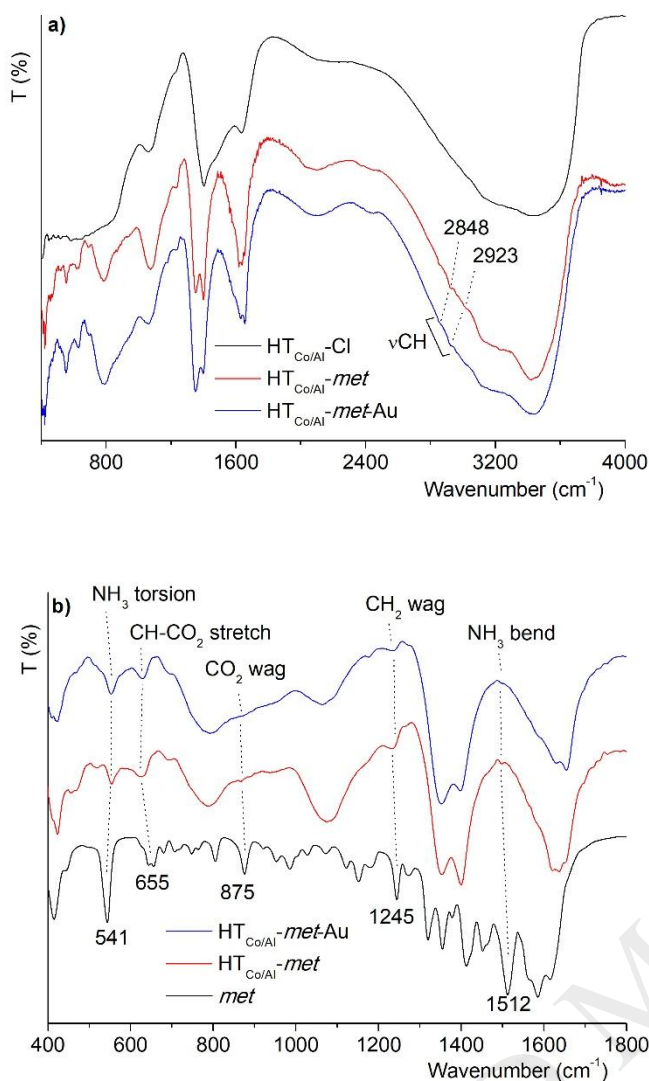


Figure 6. DRIFT spectra of $\text{HT}_{\text{Co/Al}}\text{-met}$ and $\text{HT}_{\text{Co/Al}}\text{-met-Au}$ materials. Spectra in (a) the full spectra are shown along with the spectrum of the parent $\text{HT}_{\text{Co/Al}}\text{-Cl}$ material. The νCH bands of *met* in the spectra of $\text{HT}_{\text{Co/Al}}\text{-met}$ and $\text{HT}_{\text{Co/Al}}\text{-met-Au}$ materials were marked for clearer identification. Spectra in (b) display the fingerprint region (modes below 2000 cm^{-1}) of the hybrid materials; the spectrum of *met* was included for comparison.

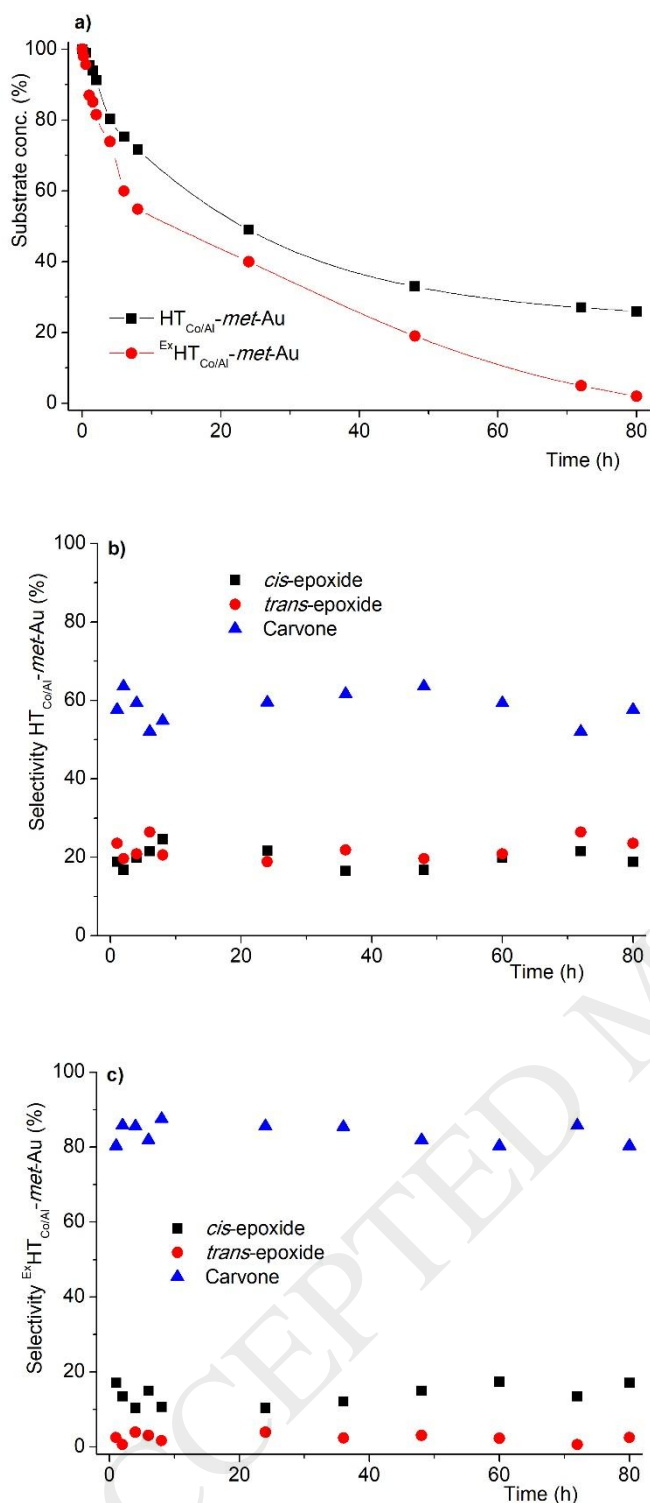


Figure 7. Reaction kinetics (a) for catalytic *R*-(+)-limonene epoxidation at 328 K with $\text{HT}_{\text{Co/Al}}\text{-met-Au}$ and $\text{Ex-HT}_{\text{Co/Al}}\text{-met-Au}$ catalysts; at the beginning there is evidence for a slight induction period compatible with a radical mechanism. Also shown are the product selectivity evolution for the bulk (b) and exfoliated (c) catalysts. It is worth noticing the difference observed for the *cis/trans* diastereomeric ratio between the bulk and the exfoliated catalysts.

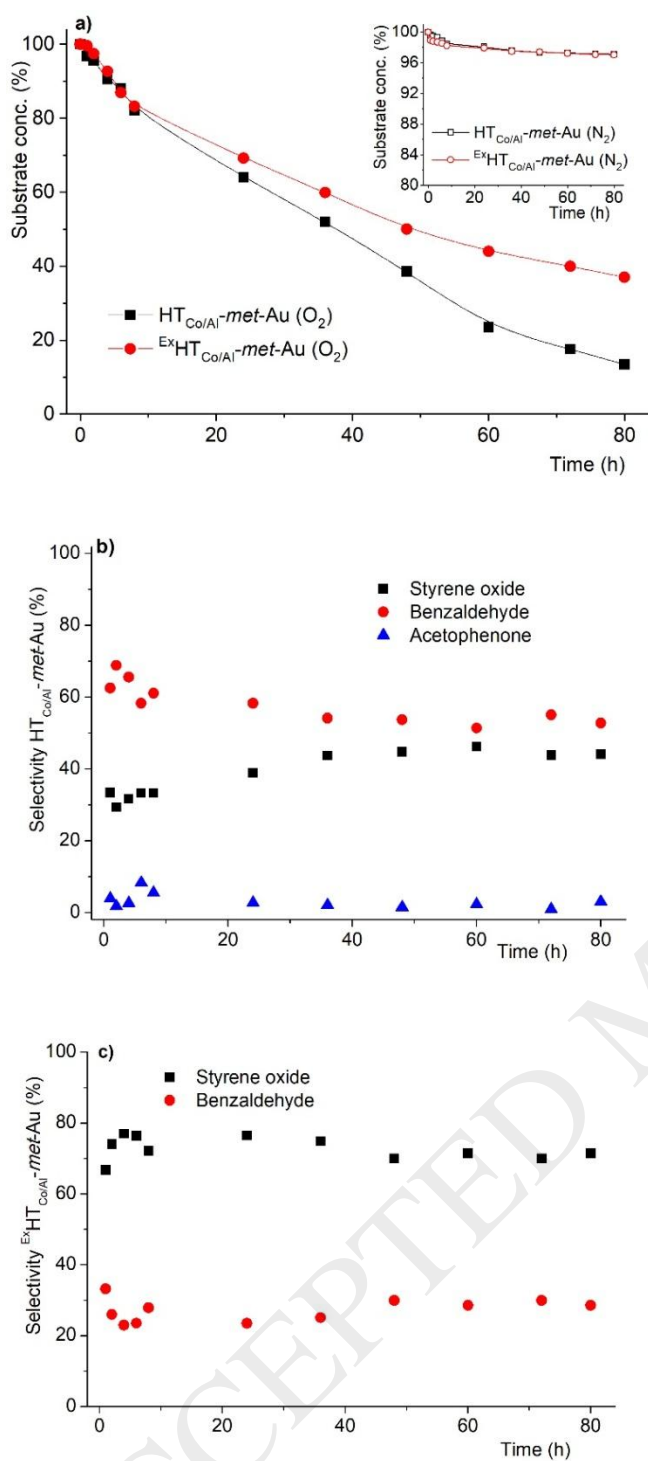


Figure 8. Reaction kinetics (a) for catalytic styrene epoxidation at 328 K under air atmosphere with $\text{HT}_{\text{Co/Al}}\text{-met-Au}$ and $\text{Ex}^{\text{HT}}\text{HT}_{\text{Co/Al}}\text{-met-Au}$ catalysts; at the beginning there is evidence for a slight induction period compatible with a radical mechanism. The inset shows the reaction kinetics performed under N_2 atmosphere, showing that O_2 is required. Also shown are the product selectivity evolution for the bulk (b) and exfoliated (c) catalysts. It is worth noticing that both catalysts displayed different major products.

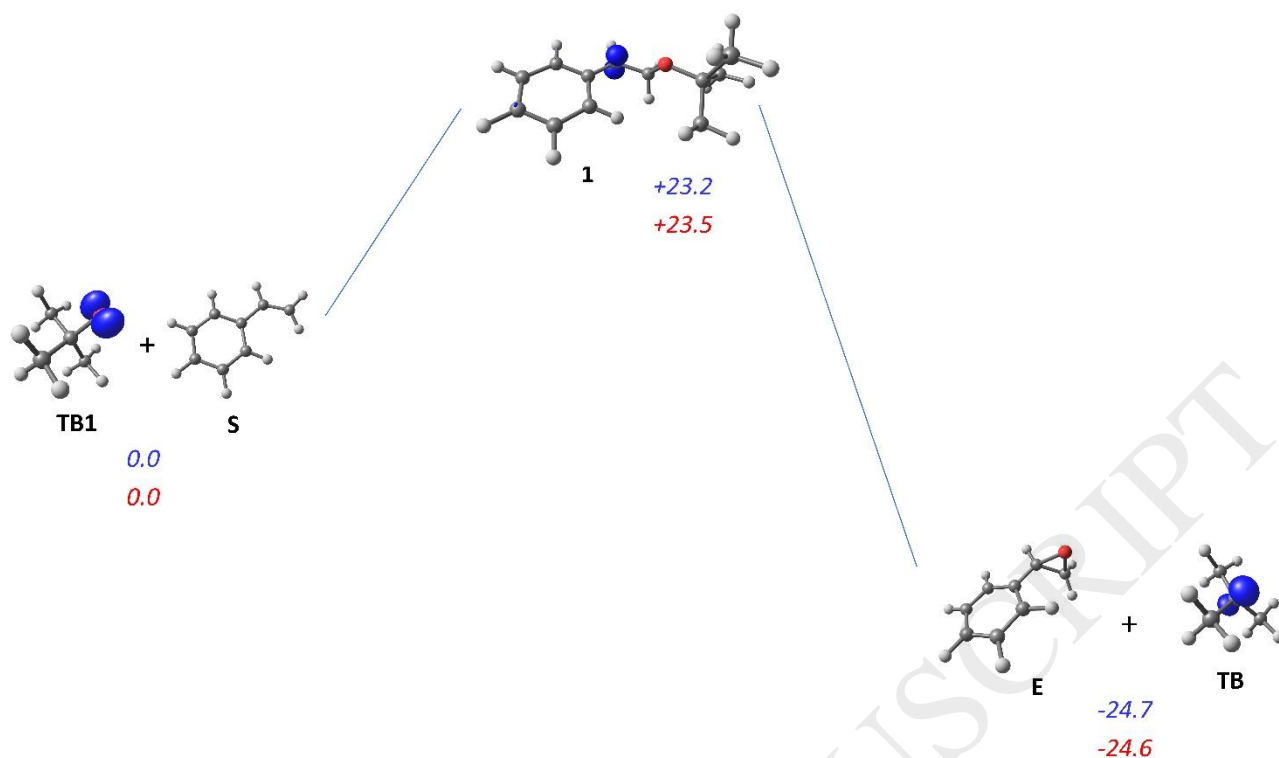


Figure 9. Free energy profile (kcal mol^{-1}) for the reaction of radical **TB1** with styrene substrate (**S**), yielding intermediary **1** and its subsequent decomposition towards the epoxide product (**E**) and radical **TB**. The top values correspond to those calculated in acetonitrile (blue) while the bottom ones were obtained for toluene (red) and are reported for the experimental reaction temperature (353 K). The spin density of the radicals was plotted in blue with a 0.05 cut-off.

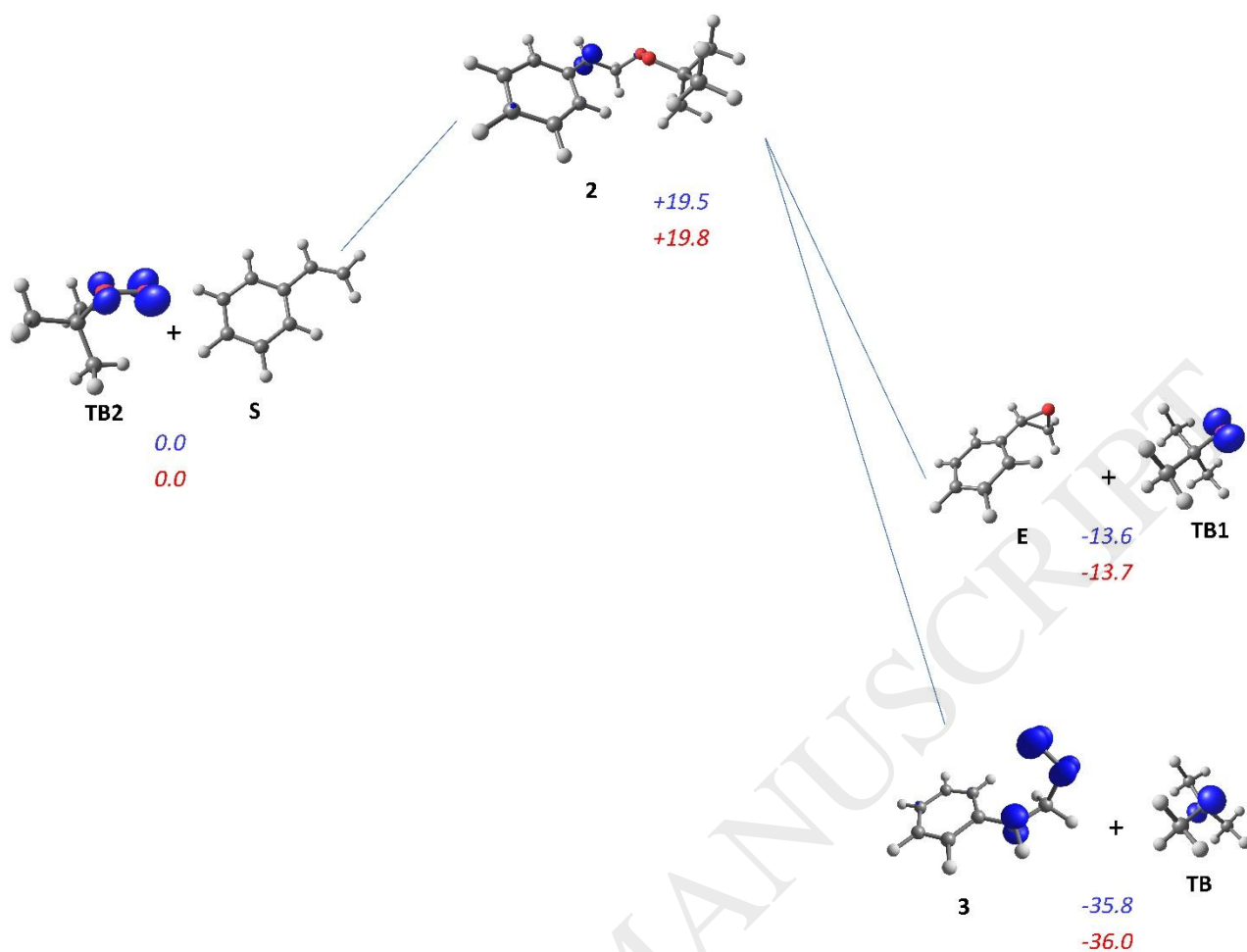


Figure 10. Free energy profile (kcal mol⁻¹) for the reaction of radical **TB2** with styrene substrate (**S**), yielding intermediary **2** and its subsequent decomposition towards the epoxide product (**E**) and radical **TB1** and the alternative pathway yielding diradical **3** and radical **TB**. The top values correspond to those calculated in acetonitrile (blue) while the bottom ones were obtained for toluene (red) and are reported for the experimental reaction temperature (353 K). The spin density of the radicals was plotted in blue with a 0.05 cut-off.

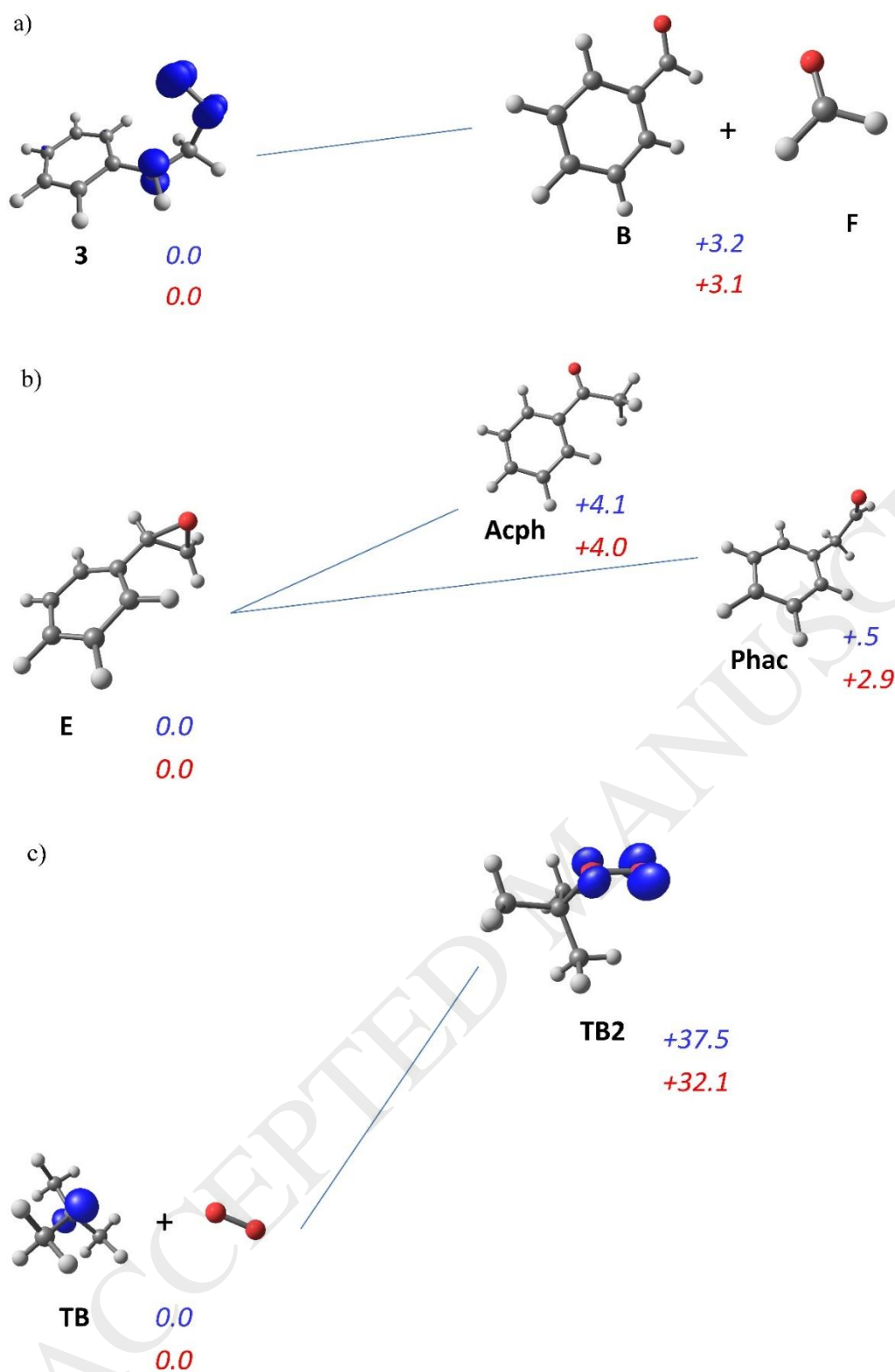
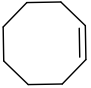

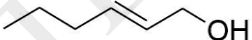
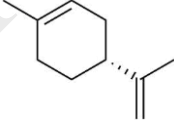
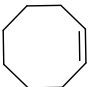
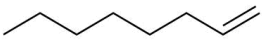
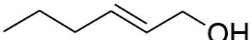


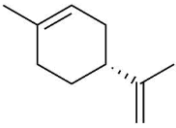
Figure 11. Free energy profile (kcal mol^{-1}) for: a) decomposition of diradical **3** towards benzaldehyde (**B**) and formaldehyde (**F**); b) isomerization of styrene epoxide (**E**) into acetophenone (**Acph**) or phenylacetaldehyde (**Phac**); c) regeneration reaction of radical **TB** with dioxygen (O_2) to yield radical **TB2**. The top values correspond to those calculated in acetonitrile (blue) while the

bottom ones were obtained for toluene (red) and are reported for the experimental reaction temperature (353 K). The spin density of the radicals was plotted in blue with a 0.05 cut-off.

ACCEPTED MANUSCRIPT

Table 1. Catalytic oxidation of different substrates using **HT_{Co/Al}-met-Au** and **^{Ex}HT_{Co/Al}-met-Au** as catalysts.

Entry	Catalyst ^[a]	Substrate	24 h		80 h	
			Conversion ^[b] (%)	Selectivity ^{[b],[c]} (%)	Conversion (%)	Selectivity ^{[b],[c]} (%)
1	HT_{Co/Al}-met-Au		62	<i>cis</i> -cyclooctene oxide: 93 cyclooct-2-ene-1-one: < 5 cyclooct-2-ene-1-ol: < 5	92	<i>cis</i> -cyclooctene oxide: 92 cyclooct-2-ene-1-one: < 5 cyclooct-2-ene-1-ol: < 5
2			9	2-hexyloxirane: 70 octan-2-one: 30	32	2-hexyloxirane: 85 octan-2-one: 15
3			42	2,3-epoxyhexan-1-ol: 87 <i>trans</i> -hex-2-enal: 13	93	2,3-epoxyhexan-1-ol: 97 <i>trans</i> -hex-2-enal: < 5
4			51	limonene-1,2-oxide: 40 (22% <i>cis</i>) carvone: 60	74	limonene-1,2-oxide: 42 (19% <i>cis</i>) carvone: 58
5	^{Ex}HT_{Co/Al}-met-Au		30	<i>cis</i> -cyclooctene oxide: 91 cyclooct-2-ene-1-one: < 5 cyclooct-2-ene-1-ol: < 5	74	<i>cis</i> -cyclooctene oxide: 96 cyclooct-2-ene-1-one: < 5 cyclooct-2-ene-1-ol: < 5
6			–	2-hexyloxirane: – octan-2-one: –	–	2-hexyloxirane: – octan-2-one: –
7			19	2,3-epoxyhexan-1-ol: 51	42	2,3-epoxyhexan-1-ol: 64

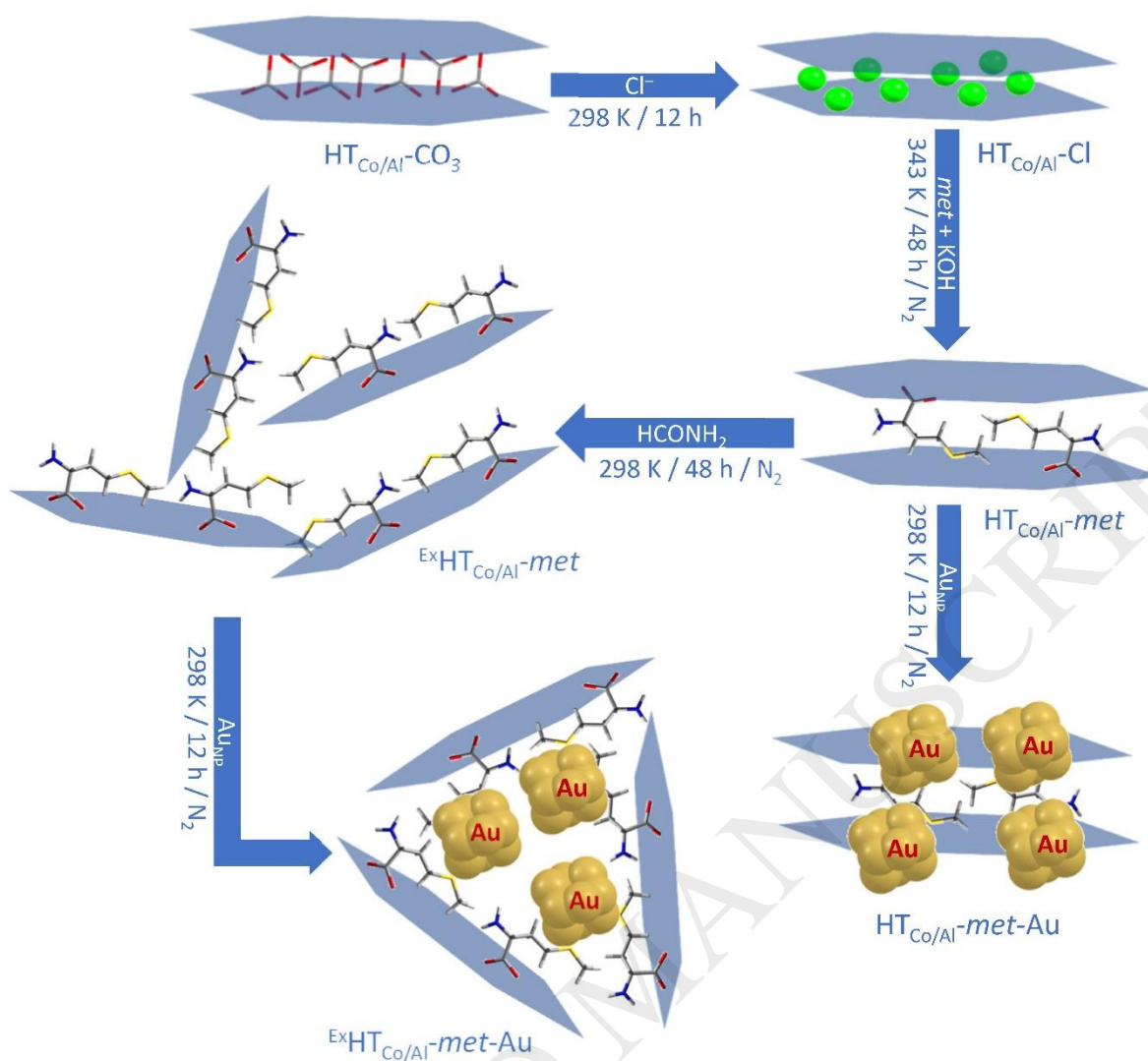
8		60	<i>trans</i> -hex-2-enal: 49 limonene-1,2-oxide: 14 (10% <i>cis</i>) carvone: 86	98	<i>trans</i> -hex-2-enal: 36 limonene-1,2-oxide: 20 (17% <i>cis</i>) carvone: 80
---	---	----	--	----	--

^[a] All reactions were carried out in the presence of 5 mol% initiator (tbhp) and 1 mol% Au catalyst; ^[b] Due to errors associated with sensitivity of measurements, very low values are reported as "< 5"; ^[c] Calculated as "Yield of epoxide"/"Conversion" × 100%; reported values are averages across different batches.

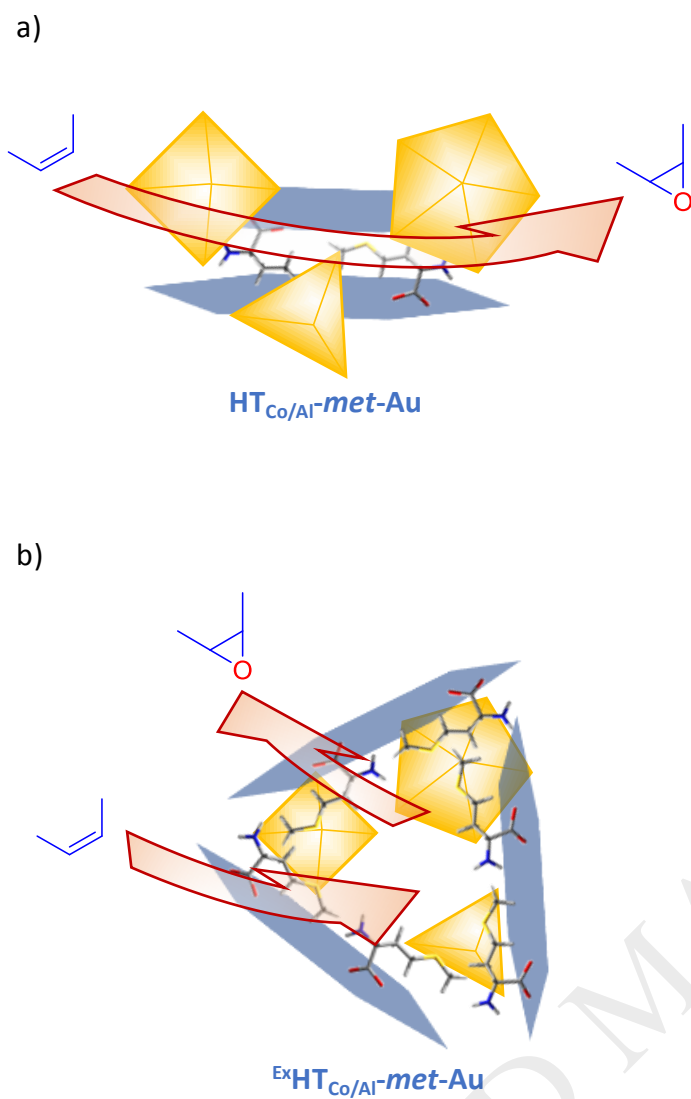
Table 2. Catalytic oxidation of styrene using **HT_{Co/Al}-met-Au** and **^{Ex}HT_{Co/Al}-met-Au** as catalysts.

Entry	Catalyst ^[a]	24 h		80 h	
		Conversion (%)	Selectivity ^{[b],[c]} (%)	Conversion (%)	Selectivity ^{[b],[c]} (%)
1	HT_{Co/Al}-met-Au	36	styrene oxide: 39 benzaldehyde: 58 acetophenone: < 5	87	styrene oxide: 44 benzaldehyde: 53 acetophenone: < 5
2	^{Ex}HT_{Co/Al}-met-Au	31	styrene oxide: 77 benzaldehyde: 23	63	styrene oxide: 71 benzaldehyde: 29

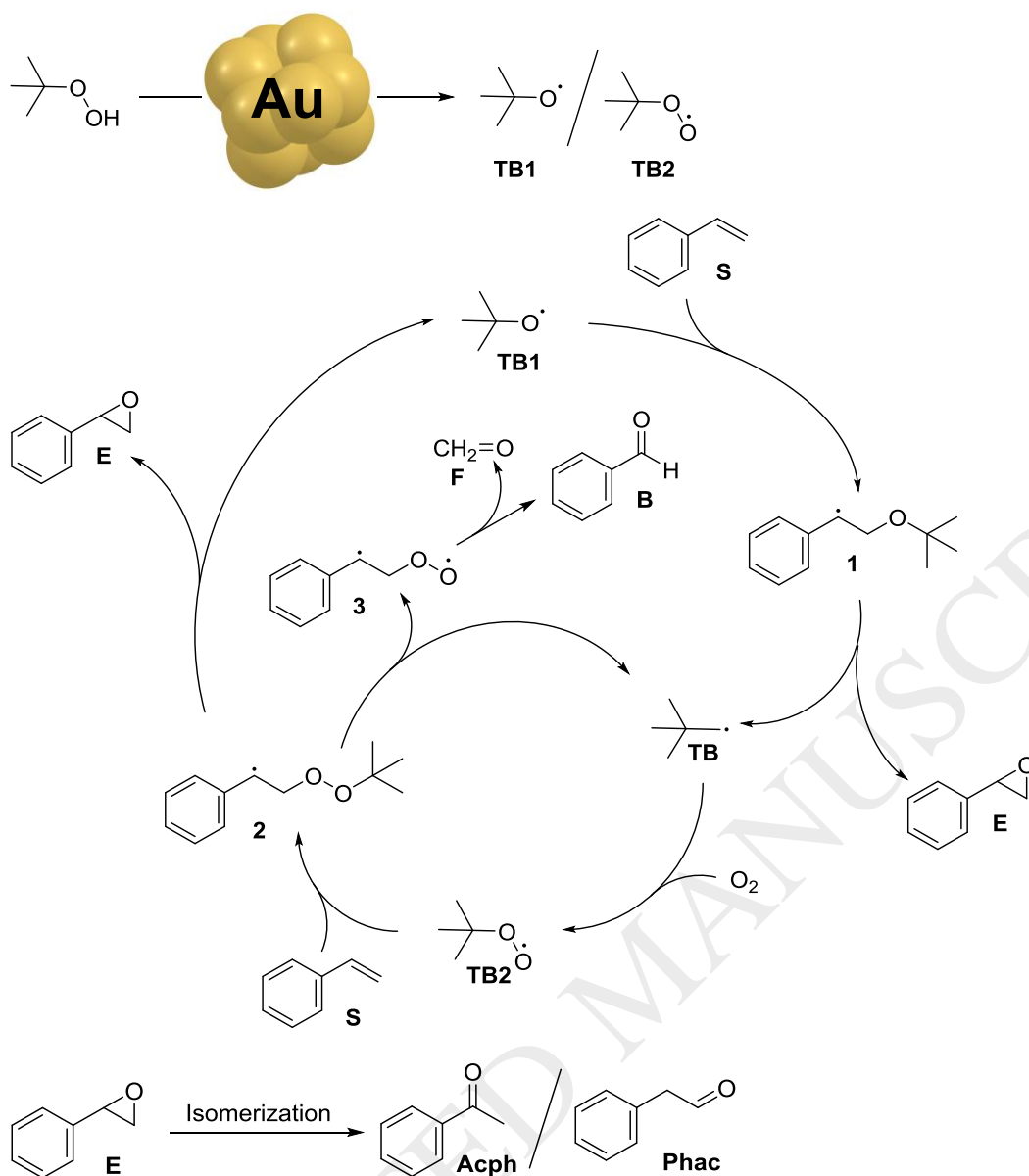
^[a] All reactions were carried out in the presence of 5 mol% initiator (tbhp) and 1 mol% Au catalyst; ^[b] Due to errors associated with sensitivity of measurements, very low values are reported as "< 5"; ^[c] Calculated as "Yield of epoxide"/"Conversion" × 100%; reported values are averages across different batches.



Scheme 1. Synthetic procedure for preparation of bulk and exfoliated $\text{HT}_{\text{Co/Al}}$ clay materials.



Scheme 2. Schematic structural differences between **HT_{Co/Al}-met-Au** (a) and **^{Ex}HT_{Co/Al}-met-Au** (b) catalysts and its implications for the catalytic process.



Scheme 3. General styrene oxidation mechanism under aerobic conditions. The different steps presented are supported by data obtained experimentally from GC-MS, and from DFT calculations.